Applied Physics Letters

PLD-derived $Ge_2Sb_2Te_5$ phase-change films with extreme bending stability for flexible device applications

Cite as: Appl. Phys. Lett. **116**, 162102 (2020); https://doi.org/10.1063/5.0001348
Submitted: 17 January 2020 . Accepted: 03 April 2020 . Published Online: 20 April 2020

Ming Li (李明), Mingzhang Xie (谢明章), Huan Ji (纪桓), Jiaoyan Zhou, Kai Jiang (姜凯), Liyan Shang (商丽燕), Yawei Li (李亚巍), Zhigao Hu (胡志高), and Junhao Chu (褚君浩)

Applied Physics Letters ARTICLE scitation.org/journal/apl

PLD-derived $Ge_2Sb_2Te_5$ phase-change films with extreme bending stability for flexible device applications

Cite as: Appl. Phys. Lett. **116**, 162102 (2020); doi: 10.1063/5.0001348
Submitted: 17 January 2020 · Accepted: 3 April 2020 ·
Published Online: 20 April 2020

View Online Export Citation CrossMark

Ming Li (李明),[1] Mingzhang Xie (谢明章),[1] Huan Ji (纪桓),[1] Jiaoyan Zhou,[1] Kai Jiang (姜凯),[1] Liyan Shang (商丽燕),[1] Yawei Li (李亚巍),[1,a)] Zhigao Hu (胡志高),[1,2,3,b)] and Junhao Chu (褚君浩)[1,2,3]

AFFILIATIONS

[1]Technical Center for Multifunctional Magneto-Optical Spectroscopy (Shanghai), Engineering Research Center of Nanophotonics and Advanced Instrument (Ministry of Education), Department of Materials, School of Physics and Electronic Science, East China Normal University, Shanghai 200241, China
[2]Collaborative Innovation Center of Extreme Optics, Shanxi University, Taiyuan, Shanxi 030006, China
[3]Shanghai Institute of Intelligent Electronics and Systems, Fudan University, Shanghai 200433, China

[a)]Electronic mail: ywli@ee.ecnu.edu.cn
[b)]Author to whom correspondence should be addressed: zghu@ee.ecnu.edu.cn

ABSTRACT

$Ge_2Sb_2Te_5$ phase-change films on flexible mica substrates are prepared by pulsed laser deposition (PLD). X-ray diffraction measurements determine the crystallographic phase of the as-deposited films and confirm that the ⟨111⟩ is the preferential orientation of growth. Temperature-dependent Raman and electrical measurements show that phase transitions from the amorphous to rock salt and hexagonal structures occur at 420 K and 550 K, respectively. Here, we have assembled a flexible electronic device with aluminum alloy sheet and silver glue for fixing after bending. Two significant resistance drops, encompassing four orders and two orders of magnitude, can be observed at the transition temperatures ranging from 420 K to 550 K. The switching ratio of the flexible devices is maintained at six orders of magnitude under different bending states. The present results demonstrate an excellent potential for applications of these PLD-deposited $Ge_2Sb_2Te_5$ films on mica substrates in flexible data storage and neuro-inspired computing.

Phase-change materials (PCMs), such as Ge–Sbe–Te alloys, are of high interest due to their advantage of nonvolatile nature, low power consumption, fast operating speed, superior temperature and mechanical endurance, high cycling endurance, and good compatibility with the complementary metal–oxide–semiconductor (CMOS) process. After the concept of using phase-change materials for memory application was first proposed by Ovshinsky and co-workers in 1968,[1] then a family of chalcogenides (Ge–Sb–Te alloys) was discovered by later researchers,[2–4] who prompted the commercialization of PCM-based optical data storage (DVDs and blue-rays) in the 1990s and subsequently the development of electrically programmable phase-change random access memory (PCRAM). Among the Ge–Sb–Te-based PCMs, $Ge_2Sb_2Te_5$ (GST) is a well-known $GeTe–Sb_2Te_3$ pseudobinary compound and possesses unique properties such as high crystallization speed (<100 ns), prominent optical reflectivity and electrical resistivity contrast, excellent reversibility, large cycling numbers of reversible transitions, and high archival lifetimes of more than 10 years for nonvolatile storage and computing applications.[5–8] Nowadays, artificial synapses for the hardware acceleration of artificial neural networks (ANNs)[8] and inline phase-change radio frequency switch (IPCS) for monolithic microwave [and millimeter-wave (MMW)] integrated circuits (MMICs)[7] are the most sought-after research hotspots among these applications.

Magnetron sputtering is typically employed for the fabrication of GST films.[9–13] As an alternative to this physical deposition method, pulsed laser deposition (PLD) has been widely used for the deposition of various complex oxides and chalcogenide films, which provides several advantages: high quality films, options for multi-compositions, quick and accurate control of the deposition process, simple deposition system, and the possibility of scaling up the process.[14–16] To date, there are only a few studies dealing with the preparation of phase-change films by PLD.[17–19] As we know, phase separation occurs

during the process of phase change from the amorphous to the crystalline states for the sputter-deposited GST films.[20] However, no phase separation of crystalline phases could be observed in the PLD-deposited GST films.[21] Meanwhile, GST films can be deposited on substrates with different thicknesses and sizes by PLD technology. To date, most of the films have been deposited on rigid substrates, such as Si and glass, which results in the fact that flexible electronic devices cannot be realized. Thus, GST films on flexible mica substrates by PLD are very promising for future flexible device applications.

In this Letter, an available nanosecond-PLD (wavelengths of 248 nm and 20 ns pulse durations) is employed as a deposition technique to fabricate GST films on flexible mica substrates. A commercial target was utilized with a Ge/Sb/Te ratio of 2:2:5. The laser beam is focused, via a plano-convex lens (focal length = 800 mm) through a quartz window, onto the surface of the rotating target at an incident angle of 60° with respect to the target normal. The pulse energy is 4 J/cm^2. The pulse repetition rate was typically set to 10 Hz with a laser pulse number of 10 000. The working pressure in the PLD chamber was typically 1.0×10^{-6} mbar during the deposition. To obtain fresh surface, original surface layers were mechanically exfoliated. These mica substrates (1×1 cm^2) were ultrasonically cleaned in ethanol and de-ionized water prior to deposition and were positioned inside the vacuum chamber parallel to the target surface at a target-to-substrate distance of 7.5 cm. The target was rotated in order to avoid deep ablation of the target and to improve the thickness homogeneity of the films. A resistive heater source is mounted in a specific position on the substrate holder, near the substrates, in order to ensure an effective thermal dissipation when increasing the substrate temperature to values required for the experiments (max. temperature of up to 1273 K). Using the above-mentioned parameters, uniform and dense films with the same thickness and size are prepared. Note that all the samples are as-deposited amorphous films except the crystalline samples studied by XRD and transmittance measurements.

The structural characteristics were analyzed by X-ray diffraction (XRD, Bruker D8 Advance diffractometer) equipped with Cu-Kα radiation ($\lambda = 0.1542$ nm). A double-beam ultraviolet–infrared spectrophotometer (PerkinElmer Lambda 950) was employed to record the normal-incident transmittance spectra in the photon energy range from 0.46 to 6.52 eV (2650–190 nm) with a spectral resolution of 2 nm. X-ray photoelectron spectroscopy (XPS, RBD-upgraded PHI-5000C ESCA system, PerkinElmer, 10 μm spot diameter) with Mg Kα radiation ($h\nu = 1253.6$ eV) was carried out to analyze the valence states and stoichiometries of the films. The Raman scattering measurements were implemented by a Jobin-Yvon LabRAM HR Evolution spectrometer (3 μm spot diameter) and a THMSE 600 heating/cooling stage (Linkam Scientific Instruments) in the range of 300–600 K. To characterize the temperature-dependent electrical properties, the resistances were measured by a Keithley model 2400 Sub-Femtoamp Remote SourceMeter and a THMSE 600 heating/cooling stage (Linkam Scientific Instruments) from 300 to 600 K.

XRD measurements were performed to clarify the crystallographic phase of GST films. The amorphous samples and the crystalline samples studied by XRD and transmittance measurements were deposited at 300 K and 473 K (the cooling rate of 10 K/min), respectively. As shown in Fig. 1(a), almost no peaks appear in the XRD spectra for amorphous GST films and the peaks from the crystalline GST

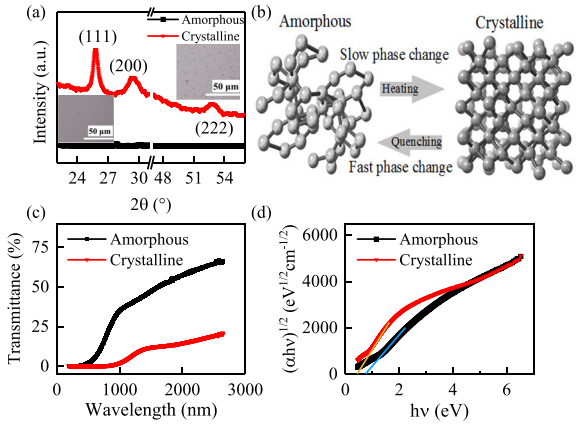

FIG. 1. (a) XRD patterns of the amorphous and the crystalline GST films. The insets show the respective surface morphologies. Note that several small crystalline regions are observed in the crystalline GST film surface morphology, which cannot be found in the amorphous GST. (b) The phase transition between the amorphous and the crystalline GST. (c) Transmittance spectra of the amorphous and the crystalline GST. (d) Curves of $(\alpha h\nu)^{1/2}$ vs photon energy derived from the data in transmittance spectra.

(25.78°, 29.38°, and 52.78°) agree with the standard database (JCPDS 54–0484), which are indexed to the (111), (200), and (222) planes of the metastable rock salt (RS) phase, respectively. The strongest XRD peak originates from (111) plane in Fig. 1(a), which is centered at around 25.78°. By comparing the relative peak intensities in the present films to the relative peak intensities derived from structural factors of bulk GST, we can conclude that the ⟨111⟩ is the preferential orientation of growth of GST films on mica. To avoid mica substrate peaks from interfering with XRD experimental results, the thickness of the samples used for XRD testing is uniform to 2 μm. The amorphous state and the crystalline state for GST films can also be distinguished visually by the change in the optical images in Fig. 1(a). Figure 1(b) illustrates the atomic rearrangements between the amorphous and the crystalline GSTs during the reversible phase transition. The amorphous structure of GST is usually assumed to possess a randomized rock salt structure without long-range order and can be sequentially crystallized into metastable rock salt and equilibrium hexagonal.[22] When the phase-change material GST is heated up by long laser pulses or long electrical pulses, the material will slowly phase change from a disordered amorphous structure to an ordered crystalline structure. Quenching is the opposite process caused by short laser pulses or short electrical pulses, while fast phase change occurs from an ordered crystalline structure to a disordered amorphous structure. As shown in Fig. 1(c), transmittance measurements were performed on both amorphous and crystalline GST films, which were significantly different. The absorption coefficient and the bandgap E_g^{opt} can be given as $\alpha = -\ln(T_{op})/d$ and $\alpha h\nu = A(h\nu - E_g^{opt})^r$, respectively. The relation $r = 2$ for indirect transitions is found to be appropriate for the crystalline GST films, giving an optical bandgap of ~0.51 eV. The Tauc–Lorentz dispersion model, also with $r = 2$, is appropriate for the amorphous GST films and gives a bandgap energy of ~0.73 eV. The difference in bandgap between the amorphous and crystalline phases is quite significant. A large concentration of vacancies generates during the crystallization process, which are apparently responsible for the very high concentrations of free carriers (~10^{20} cm^{-3}) and the decrease

in bandgap.[23] Furthermore, the high transmittance contrast between 750 nm and 2650 nm can be due to the free carrier absorption in the crystalline phases. As the infrared absorption is attributed to the charge carriers, there is a link between the optical and electrical properties.

The detailed chemical composition of GST films was analyzed by XPS technique. Figure 2(a) shows the typical overall XPS spectra of a crystalline GST film on a mica substrate. The spectra were referenced to C 1s emission at 284.6 eV. As shown in Fig. 2(b), the deconvolution of Ge 2p spectra consists of peaks at 1217.4 eV, 1220.34 eV, 1248.2 eV, and 1251.3 eV corresponding to Ge–Ge bond and Ge–Te bond in the Ge 2p orbitals, respectively. Figure 2(c) shows that the deconvolution of Sb 3d XPS peaks includes four peaks at 528.3 eV, 531.1 eV, 537.8 eV, and 540.2 eV corresponding to Sb–Sb bond and Sb–Te bond in the Sb 3d orbitals, respectively. As shown in Fig. 2(d), the Te 3d XPS peaks of Te–Te band and Te–O bond are marked at 571.9 eV, 573.3 eV, 582.4 eV, and 587.8 eV, respectively. From Fig. 2(d), the surface of the films is slightly oxidized, which does not influence its device performance. The stoichiometric ratio of Ge:Sb:Te was calculated to be 22.9:22.7:54.4, respectively, by using relative sensitivity factors, which is the same as $Ge_{2.02}$ $Sb_2Te_{4.8}$ and much close to the targeted value.

Raman scattering spectra is sensitive to the change in the crystal structures, especially local distortions and atomic substitution. Thus, Raman scattering spectra is usually used to analyze the detailed structural variation of the GST films during the phase-change process. In this work, Raman measurements were performed with a green laser at 532 nm. The laser intensity was reduced to 0.1 mW/mm^2 to avoid the laser-induced crystallization of the sample. Figure 3(a) shows the Raman spectra of the GST films with several characteristic temperatures from 300 K to 600 K. The main feature of the Raman spectra for the GST films is a broad band covering the frequency region of

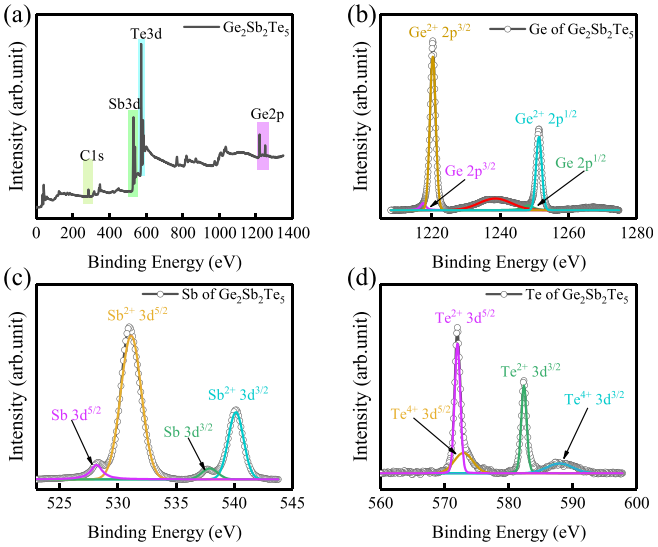

FIG. 2. (a) The overall XPS spectra of a crystalline GST film on a mica substrate. The fitted XPS spectra of (b) Ge 2p, (c) Sb 3d, and (d) Te 3d in the GST film, respectively. Note that in Fig. 2(b) the unaddressed low intensity, wide feature around 1238.5 eV, resulting from the fit over the wide range of 1208–1275 eV, does not affect the evaluation of the film stoichiometry.

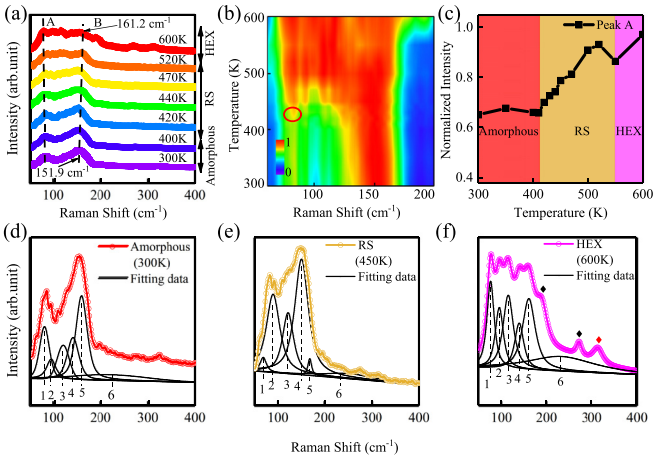

FIG. 3. (a) Temperature dependence of Raman scattering spectra for an amorphous GST film on a mica substrate with a heating rate of 10 K/min. (b) Intensity normalized contour map derived from the data in the temperature dependence of Raman spectra for the amorphous GST film. (c) Normalized intensity of peak A at 80 cm^{-1} as a function of temperature. (d)–(f) Raman spectra of amorphous GST at 300 K, RS state GST at 450 K, and HEX state GST at 600 K, including the fitting data to the Lorentz–Gaussian functions for each state. Note that the three Raman peaks with diamond markers located at around 191.7 cm^{-1}, 271.2 cm^{-1}, and 313.4 cm^{-1} at 600 K correspond to the oxide phase of Sb_2O_3 (black) and GeO (red).

50–300 cm^{-1}. The Raman spectra can be regarded as two broad peaks marked with peak A (the left dashed line) and peak B (the right dashed line), as shown in Fig. 3(a). The lower frequency peak, namely peak A, contains the F_2 mode and the E mode of the $GeTe_4$ tetrahedra vibrations. However, peak B is different between the amorphous structure and the crystalline structure. As the temperature increases, the GST film transforms from the amorphous to metastable RS phase and further crystallizes into a HEX phase. It can be found that there is a significant shift to a higher frequency (from 151.9 cm^{-1} to 161.2 cm^{-1}) of peak B during the crystallization, which is due to the gradual substitution of Sb–Te band vibrations for Te–Te band vibrations during crystallization. At the same time, the relative intensity variations of peak A present a significant change in Fig. 3(b), especially at 420 K (marked by a red circle), which is due to the enhancement of the $GeTe_4$ tetrahedra vibrations during crystallization. At the same time, we can also observe this change trend in Fig. 3(c). As shown in Figs. 3(d)–3(f), six Gaussian oscillators can be labeled as peaks 1, 2, 3, 4, 5, and 6. More evidence can be found that the intensity of peak 3 increases with increasing the temperature, which can be attributed to the increasing GeTe content in the $GeTe_{4-n}$ Ge_n ($n = 1, 2$) tetrahedra with the tetrahedra transforming into defective octahedra. The T_c from the amorphous to RS structure is estimated to be around 420 K for the amorphous GST film on a mica substrate, which is consistent with the previous works.[24] At the same time, it can be observed that there is almost no peak shift for peak A from 300 K to 600 K.

As shown in Fig. 4(c), we have assembled a flexible electronic device. After thermally evaporating the top interdigitated electrode Au (99.99%) on the amorphous GST films, we attached the backside of the GST/mica specimen onto an aluminum alloy sheet by means of silver glue. An hemispherical mold of 6.25 mm radius was employed to

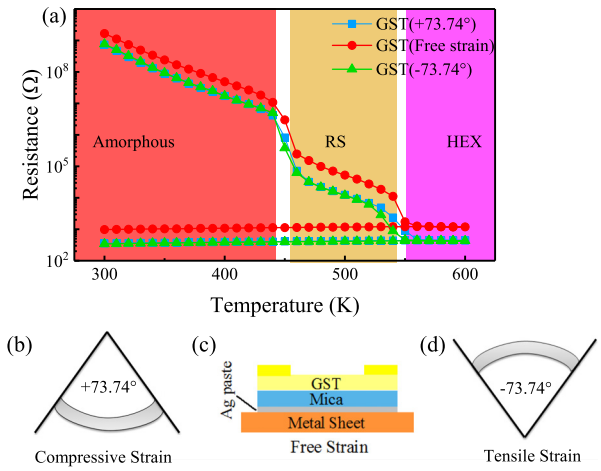

FIG. 4. (a) Temperature dependence from the resistance of the amorphous GST films with the same heating rate of 10 K/min at three kinds of strain states: compressive strain, free strain, and tensile strain. (b) and (d) schematically show the compressive and tensile strains induced by bending substrates (1 cm^2). (c) Schematic diagram of the simple flexible electronic device structure.

bend the device, inducing either compressive [= +73.74°, Fig. 4(b)] or tensile [= −73.74°, Fig. 4(d)] strain states. When the heating temperature reaches T_c (~440 K), a sharp decrease (about four orders of magnitude) in resistance is displayed, which can be associated with the amorphous–RS transformation. Then, another sharp decrease (about 2 orders of magnitude) in resistance for the GST film is observed at around 550 K, which could be due to the change from the metastable RS to a stable HE structure. Comparing the curves in Fig. 4(a), similar resistance–temperature profiles were recorded for the three strain states. At the same time, the switching ratio under the three strain states is maintained at six orders of magnitude with a set-state resistance of ~10^8 Ω and a reset-state resistance of ~10^2 Ω, which is superior than GST films prepared by magnetron sputtering.[9–13] The high electrical contrast is due to the increased free carrier density caused by the large generated concentration of vacancies during the crystallization process, consistent with the previous analysis of transmittance spectra. For the bending stability, we propose some explanations. First, compared to the generated tensile stress at T_c due to the difference in the density between the amorphous and crystalline RS phases, which can be as high as 170 MPa according to the previous reports,[25] the strain caused by bending can almost be negligible. Second, the phase separation during crystallization has been avoided, and there are no cracks appearing after bending in this work, which is different from the samples prepared by magnetron sputtering.[26] Furthermore, the GST growth on mica by PLD is a kind of van der Waals epitaxy (vdWE) growth;[27] the low stresses as the mica substrate have an atomically smooth surface, and no dangling bonds can also contribute to the bending stability.

In summary, we have deposited $Ge_2Sb_2Te_5$ phase-change films on mica by PLD. According to temperature-dependent Raman and electrical measurements, phase transition temperatures can be obtained, where the amorphous to RS and HEX structures occur at 420 K and 550 K, respectively. Moreover, the flexible electronic devices that we assembled have a high on/off ratio and excellent bending stability. The present work can contribute to the ongoing development of large scale flexible memory using these PLD-deposited GST films on mica substrates.

This work was financially supported by the Natural Science Foundation of China (Grant Nos. 91833303, 61974043, and 61674057), the National Key R&D Program of China (Grant Nos. 2018YFB0406500, 2019YFB2203400, and 2017YFA0303403), the Projects of Science and Technology Commission of Shanghai Municipality (Grant Nos. 18JC1412400, 18YF1407200, 18YF1407000, and 19511120100), and the Program for Professor of Special Appointment (Eastern Scholar) at the Shanghai Institutions of Higher Learning.

REFERENCES

[1]S. R. Ovshinsky, Phys. Rev. Lett. **21**, 1450 (1968).
[2]D. Loke, T. H. Lee, W. J. Wang, L. P. Shi, R. Zhao, Y. C. Yeo, T. C. Chong, and S. R. Elliott, Science **336**, 1566 (2012).
[3]G. I. Meijer, Science **319**, 1625 (2008).
[4]M. Wuttig and N. Yamada, Nat. Mater. **6**, 824 (2007).
[5]D. Lencer, M. Salinga, B. Grabowski, T. Hickel, J. Neugebauer, and M. Wuttig, Nat. Mater. **7**, 972 (2008).
[6]K. Ding, J. Wang, Y. Zhou, H. Tian, L. Lu, R. Mazzarello, C. L. Jia, W. Zhang, F. Rao, and E. Ma, Science **366**, 210 (2019).
[7]N. Youngblood, C. Ríos, E. Gemo, J. Feldmann, Z. Cheng, A. Baldycheva, W. H. P. Pernice, C. D. Wright, and H. Bhaskaran, Adv. Funct. Mater. **29**, 1807571 (2019).
[8]N. K. Upadhyay, H. Jiang, Z. Wang, S. Asapu, Q. Xia, and J. J. Yang, Adv. Mater. Technol. **4**, 1800589 (2019).
[9]M. H. R. Lankhorst, B. Ketelaars, and R. A. M. Wolters, Nat. Mater. **4**, 347 (2005).
[10]I. Friedrich, V. Weidenhof, W. Njoroge, P. Franz, and M. Wuttig, J. Appl. Phys. **87**, 4130 (2000).
[11]J. Pries, S. Wei, M. Wuttig, and P. Lucas, Adv. Mater. **31**, 1900784 (2019).
[12]H. J. Sun, L. S. Hou, X. S. Miao, and Y. Q. Wu, Rare Met. Mater. Eng. **39**, 377 (2010).
[13]Y. Kim, S. A. Park, J. H. Baeck, M. K. Noh, K. Jeong, M. H. Cho, H. M. Park, M. K. Lee, E. J. Jeong, D. H. Ko, and H. J. Shin, J. Vac. Sci. Technol., A **24**, 929 (2006).
[14]J. Y. Zhou, M. Z. Xie, A. Y. Cui, B. Zhou, K. Jiang, L. Y. Shang, Z. G. Hu, and J. H. Chu, ACS Appl. Mater. Interfaces **10**, 30548 (2018).
[15]M. Z. Xie, J. Y. Zhou, H. Ji, Y. Ye, X. Wang, K. Jiang, L. Y. Shang, Z. G. Hu, and J. H. Chu, Appl. Phys. Lett. **115**, 121901 (2019).
[16]H. Ji, M. Z. Xie, J. Y. Zhou, X. Wang, Z. Jin, K. Jiang, L. Y. Shang, Z. G. Hu, and J. H. Chu, Appl. Phys. Lett. **115**, 162104 (2019).
[17]H. Jiang, K. Guo, H. Xu, Y. Xia, K. Jiang, F. Tang, J. Yin, and Z. Liu, J. Appl. Phys. **109**, 066104 (2011).
[18]E. Thelander, J. W. Gerlach, U. Ross, F. Frost, and B. Rauschenbach, J. Appl. Phys. **115**, 213504 (2014).
[19]E. Thelander, J. W. Gerlach, U. Ross, A. Lotnyk, and B. Rauschenbach, Appl. Phys. Lett. **105**, 221908 (2014).
[20]S. Privitera, E. Rimini, C. Bongiorno, R. Zonca, A. Pirovano, and R. Bez, J. Appl. Phys. **94**, 4409 (2003).
[21]H. Lu, E. Thelander, Jr., W. Gerlach, D. Hirsch, U. Decker, and B. Rauschenbach, Appl. Phys. Lett. **101**, 031905 (2012).
[22]S. Guo, M. J. Li, Q. Q. Li, Z. G. Hu, T. Li, L. C. Wu, Z. T. Song, and J. H. Chu, Appl. Phys. Lett. **110**, 161906 (2017).
[23]J. K. Olson, H. Li, T. Ju, J. M. Viner, and P. C. Taylor, J. Appl. Phys. **99**, 103508 (2006).
[24]S. Guo, Z. G. Hu, X. L. Ji, T. Huang, X. L. Zhang, L. C. Wu, Z. T. Song, and J. H. Chu, RSC Adv. **4**, 57218 (2014).
[25]I. M. Park, J. K. Jung, S. O. Ryu, K. J. Choi, B. G. Yu, Y. B. Park, S. M. Han, and Y. C. Joo, Thin Solid Films **517**, 848 (2008).
[26]F. F. Schlich, A. Wyss, H. Galinski, and R. Spolenak, Acta Mater. **126**, 264 (2017).
[27]Q. S. Wang, M. Safdar, K. Xu, M. Mirza, Z. X. Wang, and J. He, ACS Nano **8**, 7497 (2014).